THE JOURNAL OF PHYSICAL CHEMISTRY C

Article

pubs.acs.org/JPCC

Implications of Transition State Confinement within Small Voids for Acid Catalysis

Andrew J. Jones,[†] Stacey I. Zones,[†,‡] and Enrique Iglesia*[,†]

[†]Department of Chemical Engineering, University of California, Berkeley, Berkeley, California 94720, United States

[‡]Chevron Energy Technology Company, Richmond, California 94801, United States

Supporting Information

ABSTRACT: The catalytic diversity of microporous aluminosilicates reflects their unique ability to confine transition states within intracrystalline voids of molecular dimensions and the number (but not the strength) of the protons that act as Brønsted acids. First-order rate constants for CH_3OH conversion to dimethyl ether (DME) reflect the energy of transition states relative to those for gaseous and H-bonded CH_3OH molecules; on zeolites, these constants depend exponentially on *n*-hexane physisorption energies for different void size and shape and proton location, indicating that van der Waals stabilization of transition states causes their different reactivity, without concomitant effects of void structure or proton location on acid strength. The dispersive contribution to adsorption enthalpies of DME, a proxy in shape and size for relevant transition states, was calculated using density functional theory and Lennard-Jones interactions on FAU, SFH, BEA, MOR, MTW, MFI, and MTT zeolites and averaged over all proton locations; first-order rate constants also depended exponentially on these enthalpies. In contrast, zero-order rate constants, which reflect the stability of transition states relative to protonated CH_3OH dimers similar in size, depended weakly on dispersive stabilization, whether measured from experiment or simulations, because dispersive forces influence species similar in size to the same extent. These results, taken together, demonstrate the preeminent effects of confinement on zeolite reactivity and the manner by which the local voids around protons held within diverse intracrystalline environments give rise to the unique behaviors that have made zeolites ubiquitous in the practice of catalysis. Enthalpic stabilization of relevant transition states prevail over entropic losses caused by confinement at low temperatures in a manner reminiscent of how catalytic pockets and solvents do so in catalysis by molecules or enzymes.

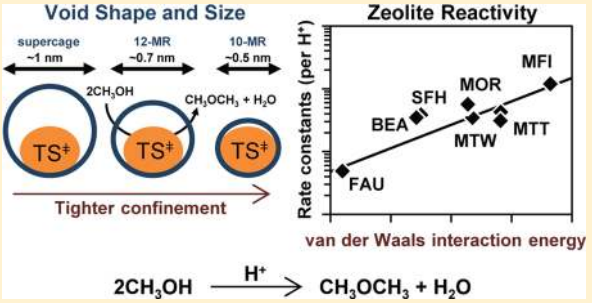

1. INTRODUCTION

Zeolite catalysts contain microporous voids that solvate transition states and reactive intermediates through van der Waals interactions and, in doing so, influence the catalytic properties of the Brønsted acid sites that reside within such voids.[1,2] These effects are evident from transition state energies derived from measured activation barriers for monomolecular cracking of C_3−C_6 *n*-alkanes on H-MFI, which decrease monotonically with increasing *n*-alkane chain size (by ∼12 kJ mol^{-1} per CH_2 group) as a consequence of van der Waals interactions that preferentially stabilize larger transition states.[2] The functional form of Gibbs free energies causes enthalpic stabilization to prevail over entropy losses caused by confinement at modest temperatures.[3−5] Measured activation barriers for C_3H_8 cracking also decrease as voids become smaller, from H-FAU (165 kJ mol^{-1},[6] ∼1.1 nm voids[7]), to H-BEA (156−159 kJ mol^{-1},[6] ∼0.6 nm voids[7]), and to H-MFI (147 kJ mol^{-1},[6] ∼0.5 nm voids[7]); these trends also indicate that a tighter fit imposed by the smaller voids enthalpically stabilizes C_3H_8 cracking transition states more effectively than larger voids. Yet, C_3H_8 cracking barriers differ markedly among samples with a given framework, when such samples differ in provenance or synthesis history (e.g., 147−167 kJ mol^{-1} for four different H-MOR samples[2]). Also, such barriers do not trend monotonically with void size or with the C_3H_8 adsorption energy within such voids for many zeolites (H-FAU, H-BEA, H-MOR, H-MFI, H-MWW, H-FER).[2,6] The origins of such inconsistencies remain unclear, at least in part, because of the uncertain location[8,9] and strength[10,11] of Brønsted acid sites and also because of the ubiquitous nature of diffusional artifacts in these microporous solids. Understanding the intrinsic reactivity of zeolites, and solid acids in general, requires structure−function relationships that involve accurate descriptors of acid strength and confinement.

The strength of a Brønsted acid is given by its deprotonation energy (DPE), which is required for heterolytic cleavage of its O−H bonds. DPE values can be estimated from density functional theory (DFT), but they cannot be measured. NH_3 adsorption energies (Q_{NH_3}) are often used instead as indirect proxies of acid strength;[10] their values, however, are insensitive to DPE changes expected from the substitution of Al by Fe in MFI (Q_{NH_3} = −145 ± 5 kJ mol^{-1} for both H-[Al]-MFI and H-[Fe]-

Received: May 21, 2014
Revised: July 3, 2014
Published: July 18, 2014

Scheme 1. Schematic Reaction Coordinate Diagram Depicting Transition State and Reactive Intermediates Involved in CH_3OH Dehydration and Their Relation to Measured First-Order ($E_{first}^{\ddagger}$) and Zero-Order ($E_{zero}^{\ddagger}$) CH_3OH Dehydration Rate Constants[a]

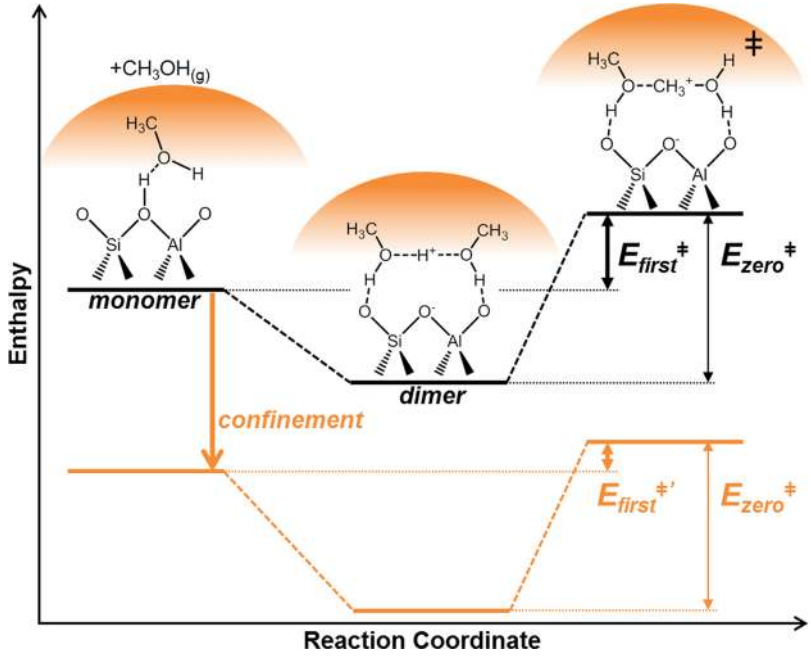

[a]H-bonded CH_3OH monomers (left) are influenced less by tighter confinement (orange) than protonated CH_3OH dimers (middle) and cationic DME formation transition states (right) because of the smaller size and number of van der Waals contacts of monomers.

Table 1. Al and H^+ Densities, Void Size Descriptors, and Origins of Zeolite Samples

zeolite	source	Si/Al ratio[a]	H^+/Al	H^+/Al[e]	pore env	D_i^f/Å	d_f^g/Å
CD-FAU	ref 17	7.5	0.37[b]	0.64	supercage	11.18	7.29
FAU	Engelhard	2.8	0.10[b]	0.15	supercage	11.18	7.29
SFH	this work	33.6	0.53[c]	0.40	14-MR	7.57	6.73
BEA	Zeolyst	11.8	0.24[b]	0.39	12-MR	6.62	6.07
MTW	this work	31.9	0.87[c]	0.63	12-MR	6.02	5.62
MOR-1	Zeolyst	10.0	0.46[c]		12-MR	6.64	6.39
MOR-2	Tosoh	9.1	0.38[c]		12-MR	6.64	6.39
MTT	this work	16.6	0.51[d]	0.46	10-MR	6.13	5.01
MFI-1	Zeolyst	16.6	0.65[c]	0.52	10-MR	6.30	4.64
MFI-2	ref 11	22.8	0.27[c]	0.33	10-MR	6.30	4.64
MFI-3	Zeolyst	29.2	0.77[c]	0.72	10-MR	6.30	4.64
MFI-4	Zeolyst	43.8	1.03[c]	0.89	10-MR	6.30	4.64
MFI-5	ref 11	51.9	0.59[c]		10-MR	6.30	4.64
MFI-6	ref 11	117.6	0.86[c]		10-MR	6.30	4.64

[a]Elemental analysis (ICP-OES; Galbraith Laboratories). [b]Titration by 2,6-di-*tert*-butylpyridine. [c]Titration by pyridine. [d]Titration by CH_3NH_2. [e]NH_3 evolution from NH_4^+-exchanged samples. [f]Largest included sphere diameter.[7] [g]Largest free sphere diameter.[7]

MFI samples,[12] which have DPE values that differ by 16 kJ mol^{-1} [11]). Q_{NH_3} values vary from 104 to 160 kJ mol^{-1} among H-MFI, H-FAU, H-CHA, and H-MOR,[13] but these trends are inconsistent with their similar DPE (1171−1200 kJ mol^{-1}, QM-Pot[13]) because Q_{NH_3} values reflect stabilization by both acid strength *and* solvation (via van der Waals interactions), which are inextricably linked; yet, Q_{NH_3} values are often interpreted—nonrigorously and inaccurately—as reflecting solely the strength of Brønsted acid sites. The measurement of acid strength, therefore, requires a systematic method for separating the contributions from acid strength and solvation to the energies of intermediates and transition states in solid acids. These methods must involve a combination of mechanistically interpreted rate data in terms of two or more rate constants that depend differently on acid strength and solvation effects.

The rate constants for elementary steps become sensitive to acid strength[14] and solvation[1,2,15] when they reflect the free energy of carbenium ion transition states relative to intermediates that differ in charge and size. At low temperatures, enthalpic effects prevail over the entropic losses inherent in confinement and electrostatic stabilization because of the functional form of Gibbs free energies. For instance, the two rate constants in the rate equations for CH_3OH dehydration on Brønsted acids reflect the energy of the transition state that mediates dimethyl ether (DME) formation relative to that of either a protonated CH_3OH dimer (k_{zero}) or a H-bonded CH_3OH and a gaseous CH_3OH molecule (k_{first}) (Scheme 1).[16] The values of these rate constants increase exponentially with

dx.doi.org/10.1021/jp5050095 | J. Phys. Chem. C 2014, 118, 17787−17800

decreasing DPE on H-MFI zeolites with different framework heteroatoms[11] and on W-based polyoxometalate clusters with different central atoms;[16] such trends reflect effects of composition on the stability of their respective conjugate bases (reflected in their DPE), which influence, in turn, the stability of the ion-pair transition states more sensitively than that of their relevant precursors. The sensitivities of k_{first} and k_{zero} depend differently on changes in DPE because of differences in charge of their respective relevant precursors (CH_3OH dimers and H-bonded species, respectively). The k_{first} and k_{zero} values also depend differently on the size of voids that contain the protons because van der Waals stabilization of DME formation transition states, CH_3OH dimers, and H-bonded CH_3OH depends on their respective different sizes. (Scheme 1)[11,16,17] The specific contributions of acid strength and solvation to such rate constants have been reported previously on H-MFI zeolites,[11] but a similar analysis has not yet been applied to other zeolite frameworks to discern the influence of zeolite structure on acid strength and the implications of solvation for these rate constants and for catalytic reactivity more generally.

Here, we report and interpret CH_3OH dehydration rate constants (normalized per accessible proton) on microporous aluminosilicates differing in framework structure and Al and proton density (H-FAU, chemically dealuminated H-FAU,[18] H-SFH, H-BEA, H-MTW, H-MOR, H-MFI, H-MTT). We relate these intrinsic reactivity measures to measured *n*-hexane adsorption enthalpies and to van der Waals interaction energies for DME adsorbed at zeolite protons derived from density functional theory (DFT) and from Lennard-Jones force-field estimates. These results provide essential mechanistic insights about how differences in acid strength and solvation among zeolites influence CH_3OH dehydration rate constants and confirm the dominant effects of solvation in the remarkable diversity of zeolites in acid catalysis.

2. METHODS

2.1. Catalyst Synthesis and Characterization. H-MFI samples (Table 1) were prepared according to protocols described previously.[11] H-MCM-41 (Sigma-Aldrich, 643653, Si/Al = 29.8), H-FAU (Engelhard, Si/Al = 2.8), NH_4^+-BEA (Zeolyst, Si/Al = 11.8), NH_4^+-MOR-1 (Zeolyst, Si/Al = 10.0), H-MOR-2 (Tosoh, Si/Al = 9.1), NH_4^+-MFI-1 (Zeolyst, Si/Al = 16.6), NH_4^+-MFI-3 (Zeolyst, Si/Al = 29.2), and NH_4^+-MFI-4 (Zeolyst, Si/Al = 43.8) samples were obtained in their H^+ or NH_4^+ forms. Chemically dealuminated H-FAU (H-CD-FAU, Si/Al = 7.5) was prepared according to protocols in the LZ-210 patent to remove extra framework Al moieties.[18,19] An aqueous $(NH_4)_2SiF_6$ solution (15000 cm^3, 99%, 1.5 M, Alfa Aesar) at 323 K was added continuously (at 1.67 g s^{-1}) to a mixture of H-USY (12 kg, Union Carbide, Si/Al = 2.9) and deionized water (36000 cm^3) at 348 K while stirring. The resulting slurry was treated to decrease the fluoride content in the samples in 1.8 kg batches by adding aqueous $Al_2(SO_4)_3$ (800 cm^3, 0.6 M) and stirring for 24 h at 368 K. The resulting solids were filtered and washed with deionized water (300 g water per 1 g zeolite) to yield NH_4-H-CD-FAU.

H-SFH was prepared by replacing B in B-SSZ-53 by Al. B-SSZ-53 was synthesized from an aqueous suspension of *N,N,N*-trimethyl-[1-(4-fluorophenyl)cyclopentyl]methylammonium hydroxide (3 mmol), NaOH (1.2 mmol, 1 M, EMD Chemicals), $Na_2B_4O_7{\cdot}10H_2O$ (0.16 mmol, Aldrich), deionized water (11.25 g), and amorphous SiO_2 (0.9 g, Cab-O-Sil M-5) treated in a rotating sealed Teflon-lined vessel (43/60 Hz, Parr, 23 cm^3) held at 433 K for 288 h in a convection oven (Blue M).[20] The resulting solids were washed with deionized water, dried at 393 K for 1 h, and then treated in flowing O_2/N_2 (0.02/0.33 cm^3 g^{-1} s^{-1}, UHP, Praxair) at 823 K (0.02 K s^{-1} to 393 K, hold 2 h, 0.02 K s^{-1} to 823 K, hold 5 h) to remove organic moieties from the voids and yield B-SSZ-53. B was replaced with Al by heating a suspension of B-SSZ-53 (0.40 g), $Al(NO_3)_3{\cdot}9H_2O$ (0.10 g) in deionized water (10 g) at 368 K for 72 h.[21] The solids were washed twice with a 0.02 M HCl solution (50 cm^3) and then deionized water (300 g water per 1 g zeolite) and finally treated in ambient air at 298 K for 24 h.

NH_4^+-MTW was synthesized by dissolving $Al(OH)_3$ (0.19 g, 53% Al_2O_3, Reheis F-2000 dried gel) in a solution of 1,4-bis(1-azoniabicyclo[2,2,2]octane)butyl dibromide (15 mmol in 25 g of water, synthesized according to previous protocols[22]), NaOH (7.7 mmol, 1 M, EMD Chemicals), and deionized water (20 g). SiO_2 (4.5 g, Cab-O-Sil M-5) was then added, and the resulting gel treated in a sealed Teflon-lined vessel (Parr, 125 cm^3) at 443 K for 132 h without stirring. The settled solids were collected by filtration, washed with deionized water (300 g water per 1 g zeolite), and treated in flowing dry air (2.5 cm^3 g^{-1} s^{-1}, UHP, Praxair) by heating to 823 K at 0.025 K s^{-1} and holding for 4 h to remove organic residues. The solids were added to an aqueous NH_4NO_3 solution (>98%, Sigma-Aldrich, 1 g zeolite per 300 cm^3 0.1 M solution) while stirring at 353 K for 4 h. The solids were recovered by filtration, and the exchange was repeated a total of three times to yield NH_4^+-MTW.

H-MTT was synthesized using reported procedures (example 1 in ref 23) by preparing a solution of *N,N′*-diisopropylimidazolium hydroxide (300 g, 1 M, synthesized according to previous protocols[24]) in deionized water (4500 g) and mixing it with a suspension containing KOH (2400 g, 1 M, Fisher), amorphous SiO_2 (1524 g, 30 wt % SiO_2, Ludox AS-30), colloidal SiO_2/Al_2O_3 (1080 g, 26 wt % SiO_2, 4 wt % Al_2O_3, Nalco 1056), and isobutylamine (150 g, >99%, Aldrich) within a Hastelloy C-lined autoclave (5 gallon, 1500/60 Hz stirring rate) and mixed for 0.5 h at 298 K. The mixture was subsequently treated by heating at 0.005 K s^{-1} to 443 K and holding for 106 h while stirring (150/60 Hz stirring rate). The solids were collected by filtration and washed with deionized water (300 g water per 1 g zeolite).

Zeolite frameworks were confirmed by X-ray diffraction (XRD; Siemens D-500; Cu Kα radiation). Si and Al contents were measured by inductively coupled plasma optical emission spectroscopy (ICP-OES; Galbraith Laboratories) and are reported in Table 1.

2.2. Catalytic Measurements. Aggregates crushed and sieved from pressed samples to retain 180−250 μm particles (0.03−0.20 g; adjusted to maintain reactant conversions <5%) were diluted with SiO_2 (Cab-O-Sil HS-5, washed with 1.0 M HNO_3, 180−250 μm aggregates, 0.2−0.5 g) and held onto a coarse quartz frit within a tubular quartz reactor (7.0 mm i.d.). The bed temperature was measured with a K-type thermocouple held in contact with the outer tube surface at the bed axial midpoint and kept constant using a three-zone resistively heated furnace (Applied Test Systems series 3210) and Watlow controllers (EZ-ZONE PM series).

All samples were treated in flowing 5% O_2/He (83.3 cm^3 g^{-1} s^{-1}, 99.999%, Praxair) by heating to 773 K at 0.025 K s^{-1}, holding for 2 h, and then cooling to 433 K before catalytic measurements. Liquid CH_3OH (99.8%, Sigma-Aldrich) was introduced into flowing He (99.999%, Praxair) through heated lines (>373 K) using a syringe pump (Cole−Palmer 780200C series). Reactant, product, and titrant concentrations were measured by gas

chromatography (Agilent 6890N GC) using a DB-Wax capillary column (0.320 mm i.d. × 30 m × 0.50 μm film; J&W Scientific) and flame ionization or mass spectrometric detection (MKS Spectra Minilab). Dimethyl ether and water were the only products detected at the conditions of these experiments.

2.3. Titration of Acid Sites by Bases. Brønsted acid site densities were measured using 2,6-di-*tert*-butylpyridine (>97%, Sigma-Aldrich), pyridine (>99.9%, Sigma-Aldrich), and CH_3NH_2 (42.9% in CH_3OH, TCI) by introducing these titrants during CH_3OH dehydration (uptakes shown in Table 1). CH_3OH dehydration turnover rates were first measured without the presence of titrants (1.1 kPa CH_3OH, 433 K) before titrant–CH_3OH mixtures were added using a syringe pump (Cole–Palmer 780200C series). The titrant concentrations in the effluent were measured using the chromatographic protocols described above. The number of protons in each sample was determined from titrant uptakes (assuming a 1:1 titrant:H^+ adsorption stoichiometry).

Brønsted acid site densities were also measured from the evolution of NH_3 from NH_4^+-exchanged samples during their thermal treatment. Samples (H^+ and NH_4^+ forms) were treated in flowing dry air (2.5 $cm^3\ g^{-1}\ s^{-1}$, UHP Praxair; heating to 823 K at 0.025 K s^{-1}, 4 h hold) and cooled to 298 K. The treated samples were transferred in ambient air to solutions of 0.1 M NH_4NO_3 (>98%, Sigma-Aldrich; 1 g zeolite per 300 cm^3 solution) while stirring at 353 K for 4 h to replace H^+ with NH_4^+. The solids were recovered by filtration and the exchange process repeated two more times. After the third exchange and filtering, solids were washed with deionized water (300 g water per 1 g zeolite) and left in contact with ambient air for 12 h. These NH_4^+-exchanged samples (0.05–0.09 g) were placed within the reactor described in section 2.2 and heated to 923 K at 0.833 K s^{-1} and held for 1 h in a flowing mixture of He (2.5 $cm^3\ g^{-1}\ s^{-1}$, 99.999%, Praxair) and Ar (0.83 $cm^3\ g^{-1}\ s^{-1}$, 99.999%, Praxair, used as internal standard). NH_3 concentrations were measured by transferring the effluent flow into a mass spectrometer (MKS Spectra Minilab) through a heated Si-coated stainless steel capillary (420 K, 0.254 mm i.d., 183 cm length) positioned immediately below the samples. The intensities for NH_3 (17, 16 amu), water (18, 17 amu), and Ar (40 amu) ions were acquired every 4 s.

2.4. Infrared Assessment of Pyridine Interactions in Zeolites. The interactions of pyridine with Brønsted and Lewis acid sites were determined from the intensity of OH vibrational bands (3800–3400 cm^{-1}) and pyridinium (1545 cm^{-1}) and pyridine–Lewis acid interaction bands (1455 cm^{-1}) before and after titrant introduction.[25] Infrared spectra were collected using a Nicolet NEXUS 670 spectrometer equipped with a Hg–Cd–Te (MCT) detector in transmission mode using self-supporting wafers (~5–15 mg cm^{-2}) and a quartz vacuum cell with NaCl windows. Spectra were measured in the 4000–400 cm^{-1} range with a 2 cm^{-1} resolution by averaging 64 scans. Samples were treated by heating to 723 K (0.033 K s^{-1}) in dry air (1.67 $cm^3\ s^{-1}$, zero grade, Praxair), holding for 2 h, and then cooling to 433 K; samples were subsequently evacuated using a diffusion pump (<0.01 Pa dynamic vacuum; Edwards E02) before collecting spectra. Pyridine (99.8%, Aldrich) was purified of absorbed gases by cooling to 77 K in a closed quartz cell, evacuating, and then heating to 298 K; this procedure was repeated three times. Purified pyridine was introduced to samples held at 433 K by incremental dosing without intervening evacuation. After pyridine saturation, the sample cell was opened to an evacuated closed loop in order to incrementally evacuate the sample. All spectra and integrated areas were normalized by the intensity of the Si–O–Si overtones (2100–1750 cm^{-1}).

2.5. Zeolite Models and Density Functional Theory Methods. van der Waals interactions of DME adsorbed at protons in zeolites from density functional theory (DFT) were used as proxies for the dispersion forces prevalent at DME transition states. DME structures and energies were determined using plane-wave periodic gradient-corrected DFT methods as implemented in the Vienna ab initio Simulation Package (VASP)[26−29] and a plane-wave energy cutoff of 396 eV. All calculations were carried out using van der Waals corrections in the vdW-DF2 functional[30] and the rPW86 exchange functional[31] with a plane-wave basis set of the projector-augmented-waves (PAW) method.[32,33] A (1 × 1 × 1) γ-centered k-point mesh was used to sample the first Brillouin zone; larger k-point mesh sizes changed adsorption energies by <0.05 eV on BEA, MFI, and MTT. All atoms were relaxed until electronic energies varied by $<1 \times 10^{-6}$ eV, and the forces on all atoms were <0.05 eV $Å^{-1}$.

H-MFI structures contain straight and sinusoidal 10-MR channels (~0.40 nm ray-averaged diameter[11]) that intersect to form larger ellipsoidal voids (~0.82 nm ray-averaged diameter[11]). Atomic coordinates and unit cell parameters (2.0022 × 1.9899 × 1.3383 nm^3 and $\alpha = \beta = \gamma = 90°$) of orthorhombic MFI (0.32 Al/uc) were determined from XRD.[34] The Al12–O20(H)–Si3 and Al7–O17(H)–Si4 Brønsted acid sites (numbered according to convention[35]) were chosen for DME adsorption on MFI because they are located at the channel intersection and sinusoidal channel voids, respectively. Lattice relaxation (maintaining interaxial lattice angles) of the MFI unit cell containing Al12–O20(H)–Si3 led to a <1% increase in the volume of the unit cell (2.008461 × 1.996122 × 1.342485 nm^3) but led to negligible changes (<3 kJ mol^{-1}) in DME van der Waals interaction energies; thus, XRD lattice constants were used without relaxation for all zeolites.

H-FAU structures contain large supercage voids (1.1 nm largest included sphere diameter,[7] 8 supercages/uc) connected by 12-MR windows (0.74 nm[36]). Atomic coordinates and unit cell parameters ($a = b = c$ = 2.4345 nm and $\alpha = \beta = \gamma = 90°$) were taken from the International Zeolite Association (IZA) site.[36] The Al1–O1(H)–Si1 site (numbered according to convention[36]) was chosen to probe DME adsorption energies because the resulting proton resides in supercage voids.

H-BEA contains straight 12-MR channels (0.56–0.77 nm[36]) which intersect to form voids similar in size to the channels themselves (largest included sphere diameter ~0.66 nm[7]). Atomic coordinates and unit cell parameters (1.26614 × 1.26614 × 2.64016 nm^3 and $\alpha = \beta = \gamma = 90°$) for BEA polymorph A were taken from XRD[37] as reported in Accelrys Materials Studio.[38] The Al2–O7(H)–Si7 site (numbered according to convention[36]) contains a H^+ at the intersection of the two channels and was chosen for these studies.

H-MTT contains one-dimensional 10-MR channels (largest free sphere diameter of 0.50 nm[7]). Atomic coordinates and unit cell parameters (0.501 × 2.152 × 1.113 nm^3 and $\alpha = \beta = \gamma = 90°$) were determined from XRD[39] as reported in Accelrys Materials Studio.[38] The Al3–O6(H)–Si7 site (numbered according to convention[36]) contains a H^+ that resides in the 10-MR channel. A supercell containing three unit cells along the lattice a direction was considered in calculations to minimize interactions between periodic adsorption images.

H-MOR structures contain one-dimensional 12-MR channels (0.65 × 0.70 nm[36]) with 8-MR (0.26 × 0.57 nm[36]) side pockets. Atomic coordinates and unit cell parameters (0.18256 × 0.20534

$\times$ 0.07542 nm^3 and $\alpha = \beta = \gamma = 90°$) were obtained from the *IZA* site.[36] Protons were considered in the 12-MR channels at the O1, O4, O5, O7, and O10 (numbered according to convention[36]) positions (see Supporting Information for structure images).

2.6. van der Waals Adsorption Energies from Force Field Calculations with Lennard-Jones Potentials. van der Waals interaction energies for DME adsorbed within zeolite void structures were determined from the distances of DME atoms to framework $O_{zeolite}$ atoms using Lennard-Jones potentials[40,41] and a custom code described herein. Zeolite structures were obtained from the *IZA* site.[36] The structure and orientation of DME with respect to Si−O(H)−Al moieties in zeolites were determined from DME structures at the Al12−O20(H)−Si3 site in MFI calculated from DFT (section 2.5). The $O_{DME}-O_{zeolite}$ bond distance and $O_{DME}-O_{zeolite}-Si_{zeolite}$ dihedral angles from this DFT-derived structure were used to place DME at each crystallographically unique $O_{zeolite}$ atom; these DME structures were rotated to optimize van der Waals interactions (discussed below). DME structures and energies at $O_{zeolite}$ atoms inaccessible to a spherical probe with a diameter of 0.325 nm (e.g., CH_4) were discarded; the accessibility of O atoms to such a probe was determined from Voronoi decompositions of the zeolite void space using Zeo++.[42,43]

The orientation of DME at each unique $O_{zeolite}$ atom was determined from a nonlinear conjugate gradient optimization of van der Waals interaction energies allowing DME structures to rotate around the O_{DME} atom about three orthogonal axes. This optimization technique, which maintains $O_{DME}-O_{zeolite}$ distances, was chosen because DFT-derived $O_{DME}-O_{zeolite}$ distances were similar for all binding locations and zeolite structures (H-FAU, H-BEA, H-MFI, H-MOR, H-MTT; 0.254 $\pm$ 0.002 nm; section 2.5 and Supporting Information) and because transition states are expected to have similar distances to zeolite anions at different proton sites as the result of their ion-pair nature and the strong energetic penalties of separating charge. Structure rotations were continued until van der Waals energies decreased by <10^{-8} eV deg^{-1}.

Initial DME structures were rotated along the axis normal to the Si−O−Si plane at each $O_{zeolite}$ atom in 36° increments (0°, 36°, 72°, etc.) to ensure that minimum-energy structures were found. These DME structures were allowed to rotate and minimize their interaction enthalpies along all three orthogonal axes until van der Waals energies varied by <10^{-8} eV deg^{-1}. The structures with the most stable van der Waals interaction energies at each $O_{zeolite}$ atom in a given zeolite were averaged:

$$\langle Q_{LJ}(DME)\rangle = k_B T \ln\left(\frac{1}{N_{O\ atoms}}\sum_{i=1}^{N_{O\ atoms}} e^{Q_{LJ,i}(DME)/k_B T}\right) \quad (1)$$

where $Q_{LJ,i}$(DME) is the optimum van der Waals interaction energy of DME at $O_{zeolite}$ atom i, $N_{O\ atoms}$ is the number of accessible $O_{zeolite}$ atoms, and T is the reaction temperature.

The average given by eq 1 resembles the ensemble (exponential) average of transition state and reactive intermediate energies at different zeolite protons (and thus O atoms) reflected in the free energies of measured rates and rate constants. Measured reaction rates, $\langle r\rangle$, reflect the sum of the reaction rate at each proton:

$$\frac{\langle r\rangle}{N_{H^+}} = \frac{1}{N_{H^+}}\sum_{i=1}^{N_{H^+}} r_i \quad (2)$$

Transition state theory treatments of thermodynamically nonideal systems[44] lead to the following reaction rate dependencies on transition state free energies relative to gas-phase reactants:

$$\frac{k_B T}{h} e^{-\langle \Delta G^{\ddagger}\rangle/k_B T}\prod_j a_j^{\nu_j} = \frac{1}{N_{H^+}}\sum_{i=1}^{N_{H^+}}\frac{k_B T}{h} e^{-\Delta G_i^{\ddagger}/k_B T}\prod_j a_j^{\nu_j} \quad (3)$$

where $\Delta G_i^{\ddagger}$ is the free energy difference of the transition state relative to gas-phase reactants at proton i, and a_j and ν_j are the gas-phase activity and reaction stoichiometry of species j, respectively. The $\Delta G_i^{\ddagger}$ reflect transition state free energies relative to gas-phase reactants because transition states are in equilibrium with reactive intermediates and gas-phase species; this implies that transition states are also in equilibrium with transition states at other protons. Equation 3 simplifies to

$$\langle \Delta G^{\ddagger}\rangle = -k_B T \ln\left(\frac{1}{N_{H^+}}\sum_{i=1}^{N_{H^+}} e^{-\Delta G_i^{\ddagger}/k_B T}\right) \quad (4)$$

which closely resembles eq 1 when DME interaction energies replace free energies and protons are located at all accessible O atoms.

3. RESULTS AND DISCUSSION

3.1. Brønsted Acid Site Titrations and Contributions of Brønsted and Lewis Acid Sites to Measured CH_3OH Dehydration Rates. The number of accessible protons must be measured to express their reactivity as turnover rates, thus allowing comparisons of their reactivity among different zeolite structures. The number of protons was determined here from 2,6-di-*tert*-butylpyridine, pyridine, and CH_3NH_2 uptakes during catalysis (Table 1). All zeolites in this study are henceforth referred to by their framework type but are implicitly in their H-form. Smaller pyridine and CH_3NH_2 titrants were used when larger 2,6-di-*tert*-butylpyridine titrants, which selectively titrate Brønsted acid sites,[45] could not be used to access protons in structures with 10-MR and 8-MR windows or channels. Rates decreased linearly with the amount of adsorbed titrant and did not increase when the titrant was removed from the reactant stream (Figure 1), indicating that titrants bind irreversibly onto the acid sites that catalyze CH_3OH dehydration to DME, as shown previously on W-based polyoxometalates[16] and MFI zeolites.[11]

Pyridine interacts with Brønsted and Lewis acid sites to form characteristic infrared absorption bands at ca. 1545 cm^{-1} and ca. 1455 cm^{-1}, respectively.[25] The infrared absorption band characteristic of the pyridinium ion (1545 cm^{-1}) increased linearly, and the Brønsted ν(OH) band (3604 cm^{-1}) decreased linearly, with pyridine uptake (Figure 2) up to pyridine/Al ratios of unity, consistent with measured H^+/Al ratios of unity (Figure 1) and with the irreversible binding of pyridine to protons. The absorption band characteristic of pyridine interacting with Lewis acid sites (ca. 1455 cm^{-1}) was undetectable below pyridine/Al ratios of unity, then increased linearly with increasing pyridine pressure, and decreased upon evacuation of gaseous pyridine (Figure 2), consistent with the reversible binding of pyridine to Lewis acid sites. The reversible binding of pyridine to Lewis acid sites shows that pyridine selectively titrates Brønsted acid sites. The proton affinity of CH_3NH_2 (899 kJ mol^{-1} [46]) is significantly lower than that of pyridine (930 kJ mol^{-1} [46]), indicating that

dx.doi.org/10.1021/jp5050095 | J. Phys. Chem. C 2014, 118, 17787−17800

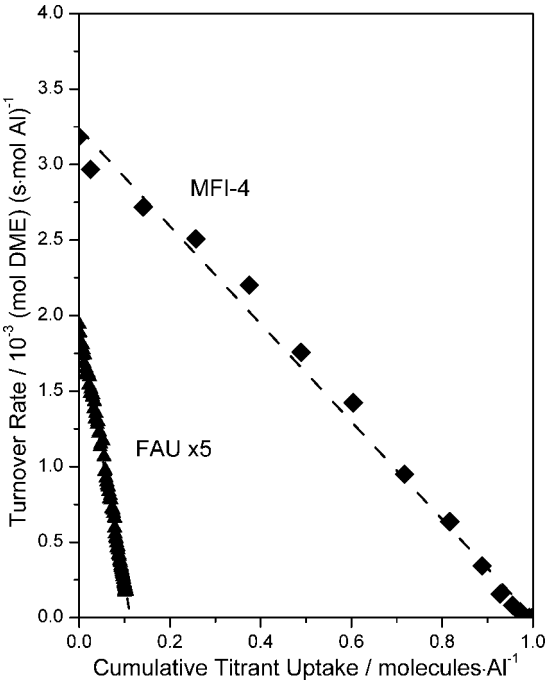

Figure 1. CH_3OH dehydration turnover rates at 433 K as a function of cumulative titrant uptake on FAU (▲; 0.5 kPa CH_3OH and 0.1 Pa 2,6-di-*tert*-butylpyridine in the feed) and MFI-4 (◆; 1.1 kPa CH_3OH and 0.4 Pa pyridine in the feed). Dashed curves are linear regressions of the data.

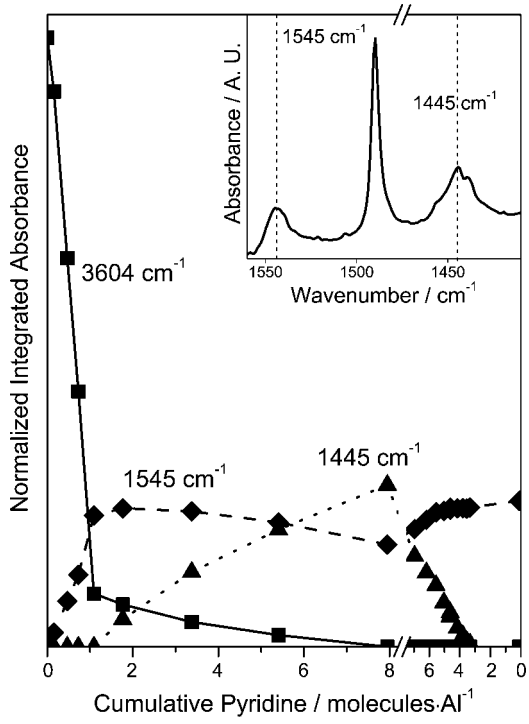

Figure 2. Integrated infrared absorbance of absorption bands characteristic of Brønsted acid ν(OH) (■; 3604 cm^{-1}), pyridinium ions (◆; 1545 cm^{-1} [25]), and pyridine interacting with Lewis acids (▲; 1445 cm^{-1} [25]) as a function of pyridine dosed (and removed) per Al on MFI-4 at 433 K. Curves are provided as a guide. Inset: infrared spectra of MFI-4 dosed with 8 pyridine/Al.

CH_3NH_2 titrants will also bind weakly and reversibly to any Lewis acid sites present in these zeolites.

2,6-Di-*tert*-butylpyridine did not fully suppress CH_3OH dehydration rates on CD-FAU, FAU (Figure 1), and BEA. CH_3OH dehydration rates after these titrations were independent of CH_3OH pressure and inconsistent with pretitration rates that were proportional to CH_3OH pressure (Supporting Information). The addition of pyridine to reactant streams after 2,6-di-*tert*-butylpyridine titrations caused rates to decrease further; these rates increased, however, when pyridine was subsequently removed from reactant streams, consistent with the presence of Lewis acid sites and with the reversible binding of pyridine onto these sites (Figure 2). These data indicate that Lewis acid sites are present and make small contributions to measured CH_3OH dehydration rates on some zeolites (CD-FAU, CD-FAU, and BEA); the reactivity of Lewis acid sites is determined from dehydration rates after titrant saturation. Brønsted acid-catalyzed turnovers were determined here by taking the difference in rates before and after titrations and correctly normalizing these rates by titrant uptakes, which reflect the number of Brønsted acid sites.

Brønsted acid site densities measured from the amount of NH_3 evolved from NH_4^+-exchanged zeolites were smaller by factors of 0.8 (MTT, SFH, and 3 MFI samples) and 0.7 (MTW) than those determined from titrations during catalysis (Table 1). NH_4^+ selectively replaces H^+ during aqueous exchange and thus probes only Brønsted acid sites. The differences in site counts among pyridine and CH_3NH_2 titrations and NH_3 evolution may reflect the adsorption of amine titrants onto Lewis acid sites; the reversibility of amine titrants on Lewis acid sites (Figure 2) and the low pressures of amines during titrations, however, preclude large contributions of these sites to measured titrant uptakes. These differences may instead reflect the hydrolysis of the zeolite framework under aqueous NH_4^+-exchange procedures, which can lead to a loss in zeolite crystallinity and a concomitant loss in the number of protons in some zeolites.[47]

NH_4^+ amounts were larger (by factors of 1.5−1.7) than 2,6-di-*tert*-butylpyridine uptakes on CD-FAU, FAU, and BEA samples. These samples have very low H^+/Al ratios (<0.37 from 2,6-di-*tert*-butylpyridine titrations) and thus a significant amount of Al outside of tetrahedral framework positions. ^{27}Al MAS NMR indicates that Al species convert from tetrahedral to octahedral coordinations, which do not have associated Brønsted acid sites, in the presence of H_2O in FAU[48] and BEA[49] structures at moderate temperatures (298−443 K) because of the hydrolysis of Al−O bonds. NH_3 adsorption reestablishes the tetrahedral coordination of some Al atoms leading to the creation of associated NH_4^+ cations, but these Al atoms revert to octahedral coordinations when NH_3 is thermally removed (723 K) and the samples are introduced to moisture at ambient conditions.[48,49] Al atoms that coordinate with NH_4^+ cations during ion-exchange procedures but do not have associated Brønsted acid sites during catalysis are consistent with the larger quantities of NH_3 than protons titrated with 2,6-di-*tert*-butylpyridine on CD-FAU, FAU, and BEA samples (Table 1). We conclude that accurate Brønsted acid site counts require titrations during catalysis.

3.2. CH_3OH Dehydration Turnover Rates and Mechanistic Interpretations of Rate Constants on Zeolites.

CH_3OH dehydration turnover rates for CD-FAU, SFH, MFI-7, BEA, and MTW are shown in Figure 3 as a function of CH_3OH pressure, with trace contributions from Lewis acid sites removed (as described in section 3.1). These data are consistent with a rate equation derived from a sequence of elementary steps proposed previously on polyoxometalates and zeolites (Scheme 2):[11,16]

dx.doi.org/10.1021/jp5050095 | J. Phys. Chem. C 2014, 118, 17787−17800

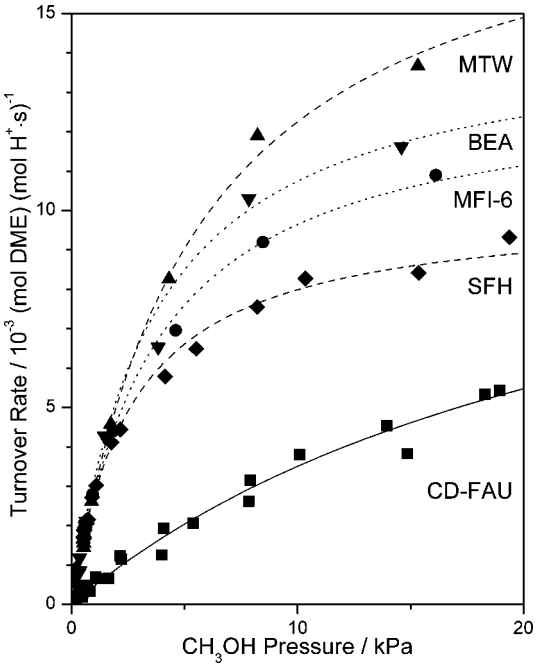

Figure 3. CH_3OH dehydration turnover rates (per H^+ determined from base titrations as indicated in Table 1; 433 K) as a function of CH_3OH pressure on CD-FAU (■), SFH (◆), MFI-6 (●), BEA (▼), and MTW (▲). Dashed curves represent regression of the data to the functional form of eq 5.

$$\frac{r_{DME}}{[H^+]} = \frac{k_{DME}K_D[CH_3OH]}{1 + K_D[CH_3OH]} = \frac{k_{first}[CH_3OH]}{1 + \frac{k_{first}}{k_{zero}}[CH_3OH]} \quad (5)$$

Scheme 2. Elementary Steps for CH_3OH Dehydration over Brønsted Acids

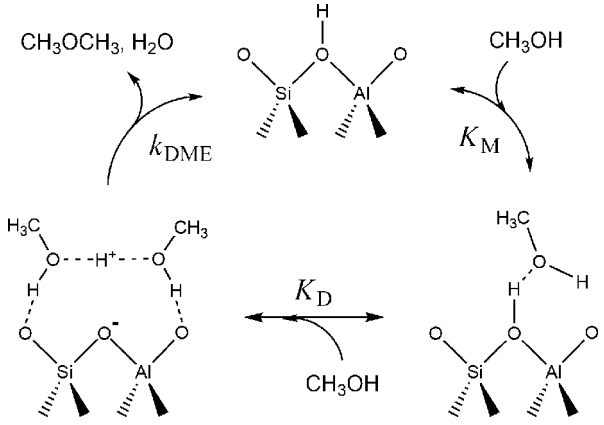

Here, k_{DME} is the rate constant for the formation of DME from protonated CH_3OH dimers, and K_D is the equilibrium constant for the formation of these dimers from H-bonded CH_3OH species. The equilibrium constant for the formation of H-bonded monomers, K_M, cancels from the numerator and denominator of eq 5. The terms in the denominator of eq 5 represent the relative concentrations of H-bonded CH_3OH monomers and CH_3OH dimers; infrared spectra during reaction have shown that these two species are the most abundant adsorbates at low and high CH_3OH pressures, respectively, on MFI, FAU, and MOR.[50] H-bonded CH_3OH monomers predominant at low CH_3OH pressures where turnover rates increased linearly with CH_3OH pressure (Figure 3) preclude dehydration turnovers that proceed through methoxide-mediated routes because these routes would lead to turnover rates that are independent of CH_3OH pressure.[11]

Equation 5 contains two rate constants (k_{first} and k_{zero}). One rate constant (k_{first}) is given by the slope of the plots in Figure 3 at low CH_3OH pressures and reflects the free energy difference between the confined DME formation transition state and a confined H-bonded CH_3OH and a gaseous CH_3OH (Scheme 1). The other rate constant (k_{zero}) reflects the asymptotic turnover rates at high pressures in Figure 3 and the free energy difference between the same confined transition state and a confined protonated dimer (Scheme 1). The values of k_{first} and k_{zero} decreased exponentially with increasing DPE values (as acid sites weakened) on W-based polyoxometalate clusters (POM) with different central atoms[16] and MFI zeolites with Al, Ga, Fe, and B heteroatoms,[11] because weaker acids require more energy to separate charge and form the required ion-pair transition states than stronger acids.[14]

The stability of ion-pair transition states and reactive intermediates depends not only on acid strength in a manner that reflects their extent of charge separation but also on the shape and size of voids, which solvate species with van der Waals interactions that depend on interaction distances ($\sim r^6$) and the identity of the atoms involved. First-order rate constants on BEA[16] and MFI[11] zeolites are larger than those expected for a (hypothetical) POM structure with similar DPE (by extrapolation of POM rate data[16]). Such reactivity enhancements by confinement reflect the preferential solvation of DME transition states over H-bonded CH_3OH monomers within these confining voids (Scheme 1). Zero-order rate constants, in contrast, are similar on zeolites with different void sizes (section 3.3) because protonated CH_3OH dimers and DME transition states are similar in size and thus in their number of van der Waals contacts with the confining framework. As a result, they are stabilized to similar extents by confinement (the approximate size of molecules and effects of confinement on activation barriers are illustrated in Scheme 1). The individual contributions of acid strength and confinement to reactivity can be interpreted from the relative values of k_{first} and k_{zero} because their values depend differently on acid strength and confinement. Next, we compare CH_3OH dehydration rate constants on a series of crystalline aluminosilicates with different framework structures to assess how differences in van der Waals stabilization influence the reactivity of solid Brønsted acids.

3.3. Consequences of van der Waals Interactions on CH_3OH Dehydration Rate Constants and the Acid Strength of Zeolites. Here, we probe how zeolite structure influences acid strength and solvation by comparing CH_3OH dehydration activation free energies (from k_{first} and k_{zero}) with enthalpies for the physical adsorption of alkanes in these zeolites. Alkane adsorption enthalpies on zeolites depend predominantly on van der Waals interactions; the additional stabilization of an alkane by a proton is much smaller than that by van der Waals contacts with an all silica framework and is similar on various zeolite frameworks (~6−10 kJ mol^{-1} on FAU and MFI frameworks).[40] Thus, alkane adsorption enthalpies serve as a convenient proxy for van der Waals interactions caused by confinement of such molecules within zeolite voids. In particular, n-C_6H_{14} molecules are of an appropriate size to probe van der Waals interactions that influence DME transition states (Figure

dx.doi.org/10.1021/jp5050095 | J. Phys. Chem. C 2014, 118, 17787−17800

5), and their adsorption enthalpies have been measured on a number of zeolite samples.[51]

Figure 4 shows first-order and zero-order CH_3OH dehydration rate constants as a function of n-C_6H_{14} adsorption

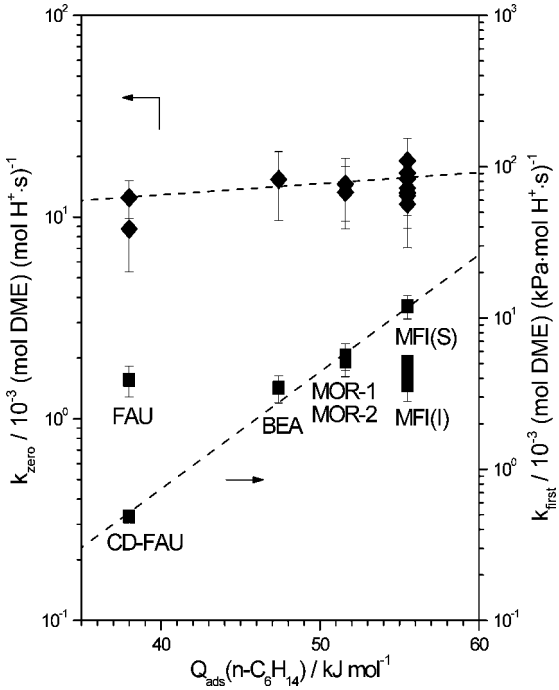

Figure 4. CH_3OH dehydration rate constants (433 K) plotted versus n-C_6H_{14} heats of adsorption[51] on protons in CD-FAU, FAU, BEA, MOR, and MFI. Two rate constants are given for MFI corresponding to those samples where H^+ are located in the channel intersection void (I; average of rate constants of MFI-2 to MFI-6) or the sinusoidal channel (S; MFI-1) as indicated in our previous work[11] and discussed herein. Dotted lines are provided to guide the eye.

enthalpies ($-Q_{ads}$(n-C_6H_{14}), microcalorimetry at 423 K[51]) on CD-FAU, BEA, MOR, and MFI zeolites. First-order rate constants increased exponentially with increasing Q_{ads}(n-C_6H_{14}) (25-fold for Q_{ads} from 38 to 56 kJ mol^{-1}; Figure 4). Zero-order rate constants, in contrast, were quite similar and were much less sensitive to Q_{ads}(n-C_6H_{14}) values (Figure 4), indicating that acid strength is similar in these zeolites, given the exponential dependence of k_{zero} values on DPE.[11,16] These similar zero-order rate constants also show that van der Waals interactions stabilize DME formation transition states and protonated CH_3OH dimer species comparably because the shape, size and number of van der Waals contacts are similar for these two species (Scheme 1).

First-order rate constants differed by a factor of ~25 among these zeolites (Figure 4) and increased exponentially (except for MFI(I) and FAU, as discussed below) with increasing values of Q_{ads}(n-C_6H_{14}). We conclude from this trend that smaller voids, which solvate n-C_6H_{14} more effectively than larger voids, also solvate DME transition states more effectively than smaller H-bonded CH_3OH species because of the larger size and number of van der Waals contacts for these transition states than H-bonded CH_3OH (Scheme 1). The effects of Q_{ads}(n-C_6H_{14}) on k_{first} (Figure 4) indicate that (i) these Al-zeolites are similar in acid strength because DPE affects k_{first} exponentially,[11,16] but Q_{ads}(n-C_6H_{14}) values predominantly reflect van der Waals interactions, or (ii) that DPE values increase monotonically with increasing void size because increasing DPE values decrease k_{first}.[11] DFT-derived DPE values for FAU, CHA, MOR, and MFI do not change in any monotonic manner with T−O−T bond angles and do not increase with increasing void size.[13,52] A 66 kJ mol^{-1} increase in DPE from the substitution of Al heteroatoms with B in MFI resulted in a ~1000-fold decrease in the value of k_{first},[11] indicating that small DPE differences would change k_{first} appreciably and affect the trends in Figure 4. We conclude that zeolites with different frameworks and structural building blocks exhibit similar acid strengths and that their catalytic diversity predominantly reflects their nonuniform voids and the confinement of transition states within them.

The conclusion that acid strengths in zeolites are similar among different frameworks is also consistent with the similar k_{zero} values between zeolites (discussed above, Figure 4) and with the similar intrinsic activation barriers for monomolecular propane cracking on several zeolites (199 ± 11 kJ mol^{-1}, on FAU, BEA, MOR, MFI, MWW, and FER).[2,6] Barriers for monomolecular propane cracking reflect differences in enthalpy between transition states and alkanes that are similar in size and which are both confined within the zeolite voids. DFT-derived DPE estimates for different zeolite frameworks, however, differ by as much as 30 kJ mol^{-1} (QM-Pot).[13] These DPE values are inconsistent with the larger k_{first} values measured on MFI (1200 kJ mol^{-1}) than on CD-FAU (1171 kJ mol^{-1}) because larger DPE values lead to smaller values of k_{first}.[11,16] DFT-derive DPE values, however, are calculated on single crystallographically unique Al−O(H)−Si sites and do not reflect the locations and distributions of protons in zeolite samples. Rate constants, in contrast, reflect the exponential average of free energy differences of transition states with reactive intermediates at all accessible proton locations allowed from Al-atom distributions (section 2.6). The difference in DPE values calculated with DFT methods, not reflected in k_{first} trends, may also reflect errors in the approximations of DFT methods, which require models for periodic zeolite structures.

First-order rate constants reflect the average van der Waals stabilizations of transition states and reactive intermediates at each proton; thus, k_{first} values are an indicator of the locations of acid sites in zeolite voids of different size and shape. The rate constants labeled MFI(S) and MFI(I) in Figure 4 refer to the MFI sample with the highest Al content (Si/Al = 16.6, MFI-1) and to another five MFI samples with lower Al content (Si/Al = 22−118, MFI-2 to MFI-6), respectively.[11] MFI(S) shows larger k_{first} values than MFI(I) samples, but similar k_{zero} values. MFI(S) also shows an infrared band (at 3656 cm^{-1}) in addition to that corresponding to the acidic OH groups present in all MFI(I) samples (at 3604 cm^{-1}). These data, taken together, indicate that some protons in MFI(S) are located in a different and more confined space than in MFI(I) because larger k_{first} are consistent with increased confinement. These results led to the previous conclusion that some protons reside within straight and sinusoidal channels, instead of larger intersections, only at the highest Al contents.[11] This is consistent with k_{first} values on MFI(I) that lie below the trend line that related such constants to n-C_6H_{14} adsorption enthalpies for the other zeolites (Figure 4) because n-C_6H_{14} adsorbs preferentially within the smaller voids, where van der Waals interactions are stronger,[40] but reactions occur and transition states are stabilized only at the intersection locations where protons reside in MFI(I) samples. The predominant siting of protons at intersections (0.63 nm largest included sphere diameter[7]) in MFI(I) is also consistent with similar k_{first} values (Figure 4) for MFI(I) and BEA (0.61−0.66

dx.doi.org/10.1021/jp5050095 | J. Phys. Chem. C 2014, 118, 17787−17800

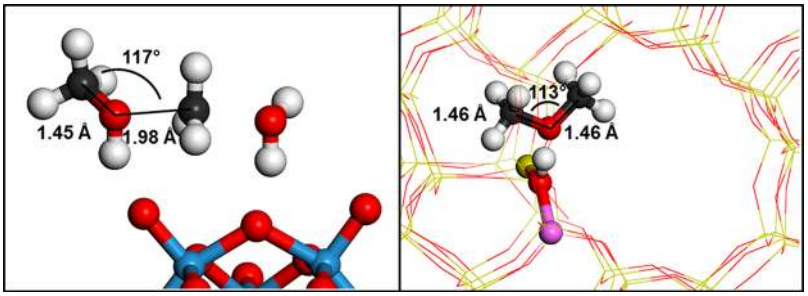

Figure 5. DME formation transition state (left), reproduced from Carr et al.[16] on HAlW, compared with DME adsorbed in MFI at Al12−O20(H)−Si3 (right) calculated at the vdW-DF2/PAW level of DFT. Atom colorings are red (O), yellow (Si), purple (Al), white (H), blue (W), and charcoal (C).

nm largest free and included sphere diameters[7]) because of the similar sizes of these voids.

The larger values of k_{first} (but not of k_{zero}) on FAU (8-fold higher) relative to CD-FAU are also indicative of the tighter confinement of transition states in FAU, in spite of the identical framework structure of these two samples. CD-FAU was prepared by treating FAU with $(NH_4)_2SiF_6$ to remove any extraframework Al debris formed during steam treatment (section 2.1). FAU contains only one crystallographically unique Al-atom position and protons that are accessible to DME transition states are contained in the supercage void (1.1 nm[7]). The smaller k_{first} on CD-FAU than on other zeolites (Figure 4) reflects the weak van der Waals stabilization of DME formation transition states within the large debris-free FAU supercages. The larger k_{first} values for FAU than for CD-FAU are due to detrital Al species (absent in CD-FAU), which occlude some of the volume of the supercages, making them more effective in confining precursors and transition states, as proposed earlier to account for higher isobutane cracking turnover rates on FAU than on CD-FAU.[17]

The comparable k_{first} values for BEA (intersecting 12-MR straight channels), MOR (1D 12-MR channel), and MFI(I) (intersecting straight and sinusoidal 10-MR channels, with H^+ at intersections) reflect the similar size of these voids and their confinement of transition states and relevant precursors. The exact location of protons at distinct O atoms in these samples, however, is unclear from these trends, in part, because n-C_6H_{14} adsorption enthalpies reflect an average of van der Waals interactions at many O atoms. The assessment of van der Waals interactions relevant to measured rate constants, therefore, requires theoretical treatments of transition states, or appropriate surrogates, at each proton. DFT calculations of van der Waals interactions of DME in zeolites are discussed next and compared with measured rate constants.

3.4. DFT-Derived DME Binding as a Probe for van der Waals Stabilization of DME Formation Transition States.

van der Waals stabilization of molecular structures reflects the location of the proton involved. Experiments cannot probe such interactions at specific locations because adsorption measurements average over all accessible locations, but such location-specific properties can be probed by theory for known structures. Here, we estimate such interactions at different O atom locations using DFT-derived DME van der Waals interaction energies and compare these with the 25-fold differences in CH_3OH dehydration rate constants in zeolites (FAU, BEA, MOR, MFI, and MTT) that reflect free energy differences of DME transition states and relevant precursors.

DFT methods have shown that CH_3OH dehydration is mediated by late and loose transition states that resemble a protonated DME molecule interacting with a nearly neutral $-OH_2$ molecule (Figure 5).[16] Bond distances and angles in DME molecules and these transition states (Figure 5) suggest that the former would capture the essential van der Waals interactions in confined transition state structures. The use of DME as a surrogate for these transition states avoids the computational intensity of transition state search algorithms at each location and allows representative samples of all accessible locations in a given framework. DME interaction energies, however, do not accurately reflect the charged nature of the transition state, its precise location within a void, or any stabilization by the $-OH_2$ moiety, all of which may influence these van der Waals interactions. Yet, the relation between DME formation rate constants and van der Waals stabilization of DME verify the value of the latter as a descriptor of reactivity.

Figure 6 shows measured CH_3OH dehydration rate constants (FAU, BEA, MOR, MFI, and MTT) as a function of DFT-derived van der Waals interaction energies for DME (Q_{vdw}(DME)) at individual acid sites determined from the

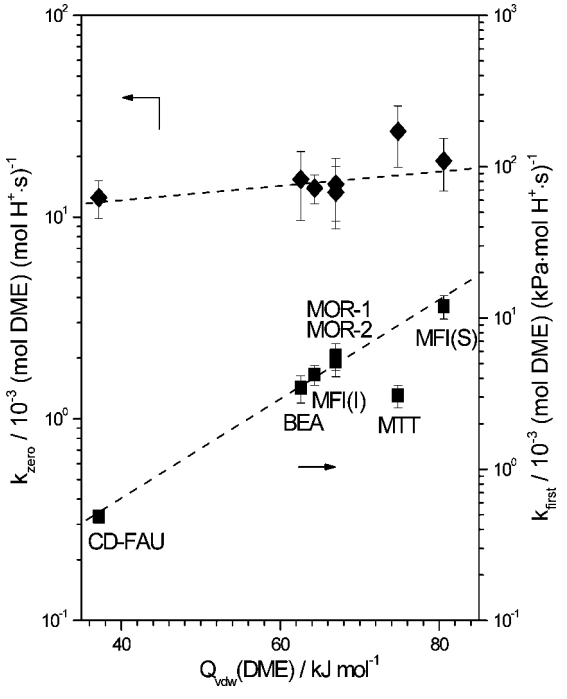

Figure 6. CH_3OH dehydration rate constants at 433 K as a function of DFT-derived DME van der Waals adsorption energies calculated at H^+ in FAU (CD-FAU), BEA, MTT, and MOR and at H^+ located in the channel intersection void (I) and the sinusoidal channel (S) of MFI. Dotted lines are provided to guide the eye.

dx.doi.org/10.1021/jp5050095 | J. Phys. Chem. C 2014, 118, 17787−17800

Table 2. Nondispersive (Q_{nd}(DME)) and Dispersive (Q_{vdw}(DME)) Portions of DFT-Derived DME Adsorption Energies (Q(DME) = Q_{nd}(DME) + Q_{vdw}(DME)) Compared with First-Order CH_3OH Dehydration Rate Constants at 433 K

zeolite	$k_{first}/10^{-3}$ (mol DME) (kPa mol H^+ s)$^{-1}$	Q_{nd}(DME)[a] (kJ mol^{-1})	Q_{vdw}(DME)[a] (kJ mol^{-1})	Q(DME)[a] (kJ mol^{-1})
CD-FAU	0.49 ± 0.04	47	37	84
BEA	3.5 ± 0.7	53	63	116
MOR-1	5 ± 1	11	67	78
MOR-2	6 ± 1	11	67	78
MFI-I	4.2 ± 0.6	78	64	143
MFI-S	12 ± 2	39	81	120
MTT	3.1 ± 0.5	113	75	188

[a]Calculated with the vdW-DF2 functional.[30]

dispersive component of DME binding enthalpies from periodic-DFT methods with vdW-DF2 functionals (section 2.5). These functionals accurately reflect van der Waals interactions and bonding interactions over large distances, indicated by potential-energy curves calculated for a range of molecule−molecule interactions that agree with quantum chemical calculations at the coupled-cluster level of theory.[30] The rate constants labeled MFI(S) and MFI(I) in Figure 6 refer to high Al content MFI (Si/Al = 16.6, MFI-1) and the average of five MFI samples with lower Al content (Si/Al = 22−118, MFI-2 to MFI-6), respectively; Q_{vdw}(DME) values were calculated for DME adsorbed in the sinusoidal channel and the intersection void of MFI structures (sections 2.5 and 3.3). Measured k_{first} values increased exponentially with increasing Q_{vdw}(DME) values (Figure 6), except for MTT (discussed below), consistent with van der Waals interactions as the predominant descriptor of reactivity differences among zeolites (section 3.3). DME binding enthalpies with van der Waals interaction contributions removed (Q_{nd}(DME) = Q(DME) − Q_{vdw}(DME)), in contrast, do not trend monotonically with k_{first} (Table 2) because nondispersive interactions depend on the orientation and overlap of molecular orbitals and do not reflect the nonspecific nature of van der Waals interactions that dominate reactivity differences.

DFT-derived DME interaction energies were calculated from the energy of DME interaction at a single proton (proton locations are discussed in section 2.5); therefore, they do not reflect the diversity of confining environments of protons in each structure, all of which contribute to measured rate constants. FAU contains one crystallographically distinct tetrahedral site (T-site) and four crystallographically distinct O atoms;[36] three of those O atoms would lead to protons within the uniform solvating environment of the FAU supercage voids and one in the sodalite cage which is inaccessible to DME molecules. As a result, the van der Waals component of DME interaction energies at Al1−O1(H)−Si1 sites (using established nomenclature[36]) in the supercage is the smallest among all zeolites (37 kJ mol^{-1}; Table 2) because of the large size of supercage voids (1.1 nm^7) and the correspondingly larger distances between framework atoms and the DME molecule than calculated in zeolites with smaller pores. BEA contains nine crystallographically distinct T-sites and 17 unique O atoms[53] with accessible binding sites (section 2.6) located in the 12-MR channels (∼0.60 nm^7) and in their intersections (∼0.66 nm^7), which are similar in size. Adsorption of DME at the Al2−O7(H)−Si7 site[36] located at the intersection of the channels in BEA results in a factor of 1.7 larger Q_{vdw}(DME) (63 kJ mol^{-1}; Table 2) than for FAU, reflecting the tighter confinement within these 12-MR channels than in FAU supercages, consistent with the larger k_{first} values in BEA than in FAU (Figure 6).

MTT structures contain 10 distinct O-sites, but only 5 are in the one-dimensional 10-MR channels accessible to DME.[36] DME binding at Al3−O6(H)−Si7 sites[36] in these 10-MR channels occurs with a larger Q_{vdw}(DME) (75 kJ mol^{-1}; Table 2) than in BEA or FAU, as a result of the smaller size of the confining environment. Yet, first-order rate constants in MTT resemble those in BEA (Table 2). As a result, k_{first} values do trend monotonically with Q_{vdw}(DME) (Figure 6). These discrepancies seem to reflect the distribution of Al atoms in zeolite structures, which lead, in turn, to differences in the van der Waals interactions of transition states and reactive intermediates. Q_{vdw}(DME) values calculated in MOR differ by as much as 70 kJ mol^{-1} depending on the orientation and locations of DME at 5 unique O atoms (Supporting Information), indicating that the location and distribution of protons can affect the stabilization of transition states. More accurate representations of the solvation reflected in k_{first} require a consideration of the confinement present at catalytically relevant protons. In section 3.5, force-field calculations of DME binding at all DME-accessible protons indicate that DME van der Waals interaction energies averaged over all proton sites (section 2.6) in MTT are similar to those within the 12-MR channels of MOR, indicating that the reactive consequences of proton distributions are similar to that of random distributions of protons in these samples. These calculations are discussed next for a wide variety of zeolites to assess DME van der Waals interaction energies at all crystallographically unique and catalytically relevant protons.

3.5. Influence of van der Waals Interactions and Acid Site Location on Rate Constants of CH_3OH Dehydration.

The distribution of Al atoms among T-sites in zeolites depends sensitively on synthetic procedures, but it is seldom accessible to experimental probes, except to materials, such as MOR, with very distinct intracrystalline void environments.[8,9,54] The assessment of Q_{vdw}(DME) values at all accessible O atoms in the zeolites considered here in this paper (∼100 O atoms) remains computationally prohibitive using DFT methods and unnecessary because the van der Waals component of these adsorption energies can be estimated accurately using Lennard-Jones potentials to describe interactions between confined molecules and the O atoms of the zeolite framework.[40]

Here, we employ Lennard-Jones potentials[39,40] to assess the van der Waals interactions of DME at all accessible crystallographically unique O atoms in zeolite structures (CD-FAU, BEA, SFH, MTW, MTT, MFI(S), and MOR; section 2.6). The most stable DME interaction energies at each O-site were averaged ($\langle Q_{LJ}$(DME)$\rangle$) at 433 K from the sum of Arrhenius-type exponentials containing interaction energies to reflect the averaging of transition state free energies at all Brønsted acid sites in rate constants (section 2.6). Rate constants, however,

dx.doi.org/10.1021/jp5050095 | J. Phys. Chem. C 2014, 118, 17787−17800

reflect the average of free energy differences of transition states only at O-sites where protons exist.

Figure 7 shows CH_3OH dehydration rate constants on CD-FAU, BEA, SFH, MTW, MTT, MFI(S), and MOR samples as a

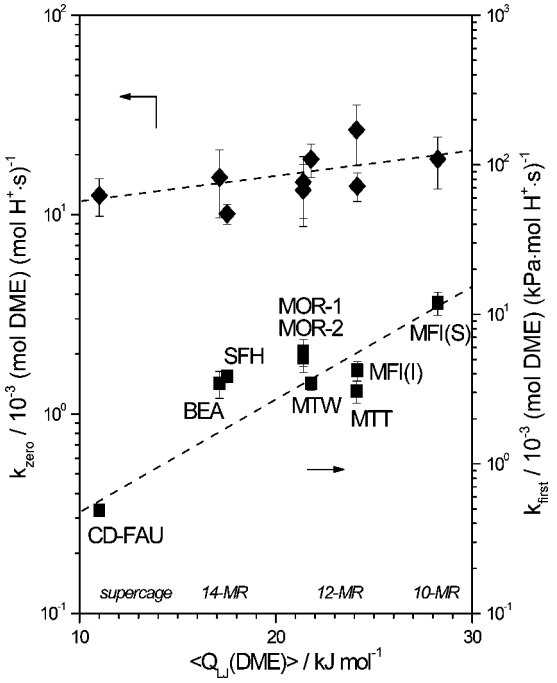

Figure 7. CH_3OH dehydration rate constants at 433 K as a function of reaction averaged (eq 1) DME van der Waals interaction energies (433 K) calculated with Lennard-Jones potentials[41] at all accessible H^+ in FAU, BEA, SFH, MTW, MTT, MOR, and MFI (MFI(S)) and for DME located in H^+ in the channel intersection void of MFI (MFI(I)). Dotted lines are provided to guide the eye.

function of $\langle Q_{LJ}(DME)\rangle$ values. The MFI(I) entry averages Waals interaction energies only for protons at intersections, whereas the MFI(S) entry averages those interactions at all accessible O-sites; the monotonic trends of rate constants with these energies (Figure 7) support the preferential siting of protons in the intersections of MFI at low Al densities (discussed also in sections 3.3 and 3.4).

First-order (but not zero-order) rate constants increased exponentially with $\langle Q_{LJ}(DME)\rangle$ values. This supports our previous conclusions that dispersive interactions dominate the reactivity differences of zeolites because $\langle Q_{LJ}(DME)\rangle$ values depend only on these nonspecific interactions. Zero-order rate constants are similar and independent of $\langle Q_{LJ}(DME)\rangle$ values because of the similar shape, size, and number of van der Waals contacts of transition states and CH_3OH dimers (Scheme 1). The fixed values of k_{zero} and the monotonic trends of k_{first} with $\langle Q_{LJ}(DME)\rangle$ also support the unchanging acid strength of zeolites with different structure, provenance, Al density, and treatments because these rate constants depend exponentially on acid strength.

$\langle Q_{LJ}(DME)\rangle$ values reflect the DME van der Waals interaction energies at all protons accessible to DME (0.325 nm diameter spherical probe; section 2.6) and makes no assumptions about the locations of protons. The monotonic trends of k_{first} versus $\langle Q_{LJ}(DME)\rangle$ in Figure 7 indicate that the reaction-averaged (section 2.6) solvation differences of transition states due to confinement are similar to those differences of $\langle Q_{LJ}(DME)\rangle$ calculated at all protons. Deviations from these trends can be explained by the preferential siting of protons due to Al atom locations fixed during synthesis or subtle differences in the way transition states structures are influenced by confinement differently than DME.

Next, we assess DME interaction energies at specific O atom locations to understand the variability of solvation environments in a given zeolite. Figure 8 shows Q_{LJ}(DME) values calculated at

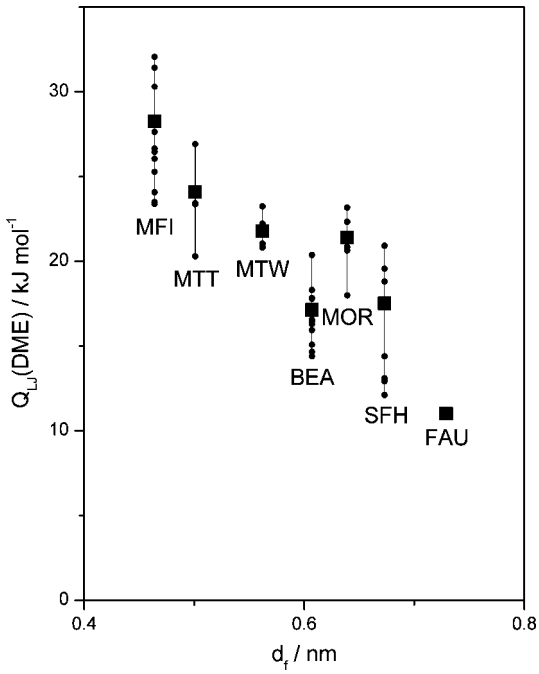

Figure 8. DME van der Waals adsorption energies with Lennard−Jones potentials[41] at all accessible protons (●) and their reaction average (433 K; eq 1; ■) plotted against largest free sphere diameters (d_f).[7]

all accessible protons and their ensemble average $\langle Q_{LJ}(DME)\rangle$ as a function of largest free sphere diameters (d_f).[7] Q_{LJ}(DME) values vary up to 9 kJ mol^{-1} (SFH) in a single zeolite and depend sensitively on the locations of protons in their voids. Thus, the distribution and location of protons can affect the solvation of transition states and precursors. $\langle Q_{LJ}(DME)\rangle$ values loosely correlate with d_f values in accordance with the r^{-6} dependence of van der Waals stabilizations. Zeolite size metrics, therefore, provide qualitative indicators of the confinement of transition states but do not necessarily reflect the distribution and variety of voids that are relevant to catalysis.

van der Waals interactions between DME and zeolite voids depend on atom identity and atom-to-atom distances, but the variance in Q_{LJ}(DME) values in a given zeolite are sometimes surprising. For example, Q_{LJ}(DME) values range from 12 to 21 kJ mol^{-1} ($\langle Q_{LJ}(DME)\rangle$ = 18 kJ mol^{-1}) at various proton-binding sites of SFH, yet DME structures are all contained within the one-dimensional 14-MR channels. The variety of Q_{LJ}(DME) values is caused by the asymmetric shape of these channels, which resemble a teardrop shape rather than a circle (Figure 9), and not binding locations in radically different environments. DME located at the wider section of these channels have higher van der Waals interaction energies because DME molecules can rotate perpendicular to channel directions to increase solvation. First-order rate constants of SFH are similar to those for MOR and MTW (Figure 7), consistent with protons located preferentially in wider sections of the 14-MR channels and the

dx.doi.org/10.1021/jp5050095 | J. Phys. Chem. C 2014, 118, 17787−17800

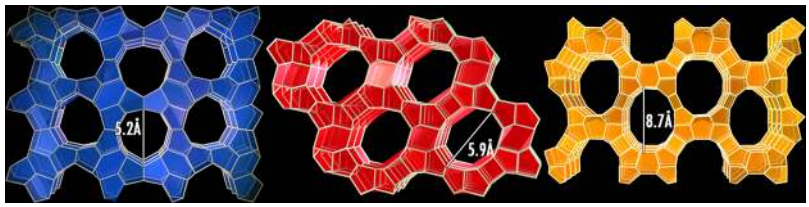

Figure 9. Depiction of one-dimensional channels in MTT, MTW, and SFH zeolites (left to right).

Q_{LJ}(DME) values there. We conclude that the shape and size of zeolite voids and the specific locations of protons among those voids are important for determining van der Waals interactions that accurately reflect those relevant to catalysis.

The exponential increases in first-order, but not zero-order, CH_3OH dehydration rate constants with measured Q_{ads}(*n*-C_6H_{14}) (section 3.3, Figure 4), calculated Q_{vdw}(DME) (section 3.4, Figure 6), and calculated $\langle Q_{LJ}(\text{DME})\rangle$ (section 3.5, Figure 7) provide compelling evidence that confinement and not acid strength differences influence the differences in stability of transition states in aluminosilicates. These results also demonstrate that van der Waals interactions influence rate constant values only when transition states and reactive intermediates differ in shape, size, and number of van der Waals contacts, as is the case for first-order, but not zero-order, rate constants. Efficient force-field calculations of transition state proxies accurately reflect the differences in van der Waals interactions due to confinement and relevant for catalysis and permit the screening of large databases of zeolite structures[55] to narrow the discovery of catalytically relevant materials with enhanced reactivity and selectivity. The success of these methods will ultimately depend on knowledge or design of the location of Al within these structures, which governs the local environment, and thus the confinement of transition states and relevant reactive intermediates.

4. CONCLUSIONS

CH_3OH dehydration rate constants, normalized rigorously by the number of protons present during reaction, reflect differences in the electrostatic and dispersive stabilization of DME formation transition states and relevant precursors. First-order CH_3OH dehydration rate constants increased exponentially with *n*-C_6H_{14} adsorption enthalpies, which depend only on differences in van der Waals interactions, consistent with reactivity differences that are dominated by differences in confinement, but not acid strength. These trends and zero-order rate constants that are independent of aluminosilicate structure indicate that Brønsted acid sites of aluminosilicates are sensibly equivalent in acid strength.

DME van der Waals interaction energies, calculated from periodic density functional theory and Lennard-Jones potentials, accurately reflect the van der Waals interactions of DME formation transition states, indicated by the monotonic increase in first-order rate constants with their values, consistent with the late DME-like structures of these transition states. DME interaction energies appropriately averaged over all accessible and crystallographically unique O atoms in zeolites also reflect the systematic 25-fold increase in first-order rate constants with tighter confinement in FAU, SFH, BEA, MOR, MTW, MFI, and MTT; these trends imply that the average solvation of transition states in zeolites reflected in rate constant values is similar to the average solvation of transition states at all O atoms for these zeolites. Deviations from these trends provide supporting evidence for the occlusion of supercage voids by detrital Al in FAU and the preferential location of protons in the channel intersections of MFI samples with Si/Al $\geq$ 22, consistent with infrared signatures of their Brønsted acid sites and similar first-order rate constant values for MFI (Si/Al $\geq$ 22) and BEA.

These findings reflect the magnitude of van der Waals interactions on the relative stability of transition states at different acid sites in zeolites. Acid strength differences of aluminosilicates are insensitive to changes in structure and depend instead on changes in the composition of framework heteroatoms. We find that nonspecific dispersive interactions, previously described as transition state shape selectivity or nest effects, are ubiquitous in microporous solid acid catalysis and, in fact, are the dominant forces that control their reactivity differences. The force-field methods described herein provide a novel method for the prediction of zeolites with enhanced reactivity and selectivity; more accurate predictions will ultimately rely on knowledge or selection of the locations and distribution of Al atoms.

These results demonstrate that the remarkable diversity in reactivity of aluminosilicate catalysts is the result of subtle changes in the size and shape of zeolite voids, which lead, in turn, to differences in the solvation of transition states and reactive intermediates. The solvation of transition states through van der Waals interactions parallels the interactions in enzyme catalysis and the solvation sphere of molecules around transition states in liquid media.

■ ASSOCIATED CONTENT

Ⓢ Supporting Information

DME adsorption structures and their energies in H-MOR from periodic-DFT, DME distances to zeolite O atoms in various structures from periodic-DFT, and further discussion of CH_3OH dehydration rates after titrations with amines. This material is available free of charge via the Internet at http://pubs.acs.org.

■ AUTHOR INFORMATION

Corresponding Author

*Fax + 1 510 642 4778; e-mail iglesia@berkeley.edu (E.I.).

Notes

The authors declare no competing financial interest.

■ ACKNOWLEDGMENTS

The authors thank Dr. Rob Carr (UC Berkeley) and Dr. Rajamani Gounder (UC Berkeley) for helpful technical discussions. Financial support from Chevron Energy Technology Company and supercomputing resources provided by the XSEDE Science Gateways program (CTS130011) are gratefully acknowledged. A.J. acknowledges a graduate research fellowship from the National Science Foundation.

REFERENCES

(1) Derouane, E. G. Shape Selectivity in Catalysis by Zeolites - the Nest Effect. *J. Catal.* **1986**, *100*, 541−544.
(2) Gounder, R.; Iglesia, E. The Catalytic Diversity of Zeolites: Confinement and Solvation Effects within Voids of Molecular Dimensions. *Chem. Commun.* **2013**, *49*, 3491−3509.
(3) Bhan, A.; Gounder, R.; Macht, J.; Iglesia, E. Entropy Considerations in Monomolecular Cracking of Alkanes on Acidic Zeolites. *J. Catal.* **2008**, *253*, 221−224.
(4) Gounder, R.; Iglesia, E. Effects of Partial Confinement on the Specificity of Monomolecular Alkane Reactions for Acid Sites in Side Pockets of Mordenite. *Angew. Chem., Int. Ed.* **2010**, *49*, 808−811.
(5) Gounder, R.; Iglesia, E. The Roles of Entropy and Enthalpy in Stabilizing Ion-Pairs at Transition States in Zeolite Acid Catalysis. *Acc. Chem. Res.* **2012**, *45*, 229−238.
(6) Xu, B.; Sievers, C.; Hong, S. B.; Prins, R.; van Bokhoven, J. A. Catalytic Activity of Bronsted Acid Sites in Zeolites: Intrinsic Activity, Rate-Limiting Step, and Influence of the Local Structure of the Acid Sites. *J. Catal.* **2006**, *244*, 163−168.
(7) Foster, M. D.; Rivin, I.; Treacy, M. M. J.; Friedrichs, O. D. A Geometric Solution to the Largest-Free-Sphere Problem in Zeolite Frameworks. *Microporous Mesoporous Mater.* **2006**, *90*, 32−38.
(8) Sastre, G.; Fornes, V.; Corma, A. On the Preferential Location of Al and Proton Siting in Zeolites: A Computational and Infrared Study. *J. Phys. Chem. B* **2002**, *106*, 701−708.
(9) Dědeček, J.; Sobalík, Z.; Wichterlová, B. Siting and Distribution of Framework Aluminium Atoms in Silicon-Rich Zeolites and Impact on Catalysis. *Catal. Rev.* **2012**, *54*, 135−223.
(10) Gorte, R. J. What Do We Know About the Acidity of Solid Acids ? *Catal. Lett.* **1999**, *62*, 1−13.
(11) Jones, A. J.; Carr, R. T.; Zones, S. I.; Iglesia, E. Acid Strength and Solvation in Catalysis by MFI Zeolites and Effects of the Identity, Concentration and Location of Framework Heteroatoms. *J. Catal.* **2014**, *312*, 58−68.
(12) Parrillo, D. J.; Lee, C.; Gorte, R. J.; White, D.; Farneth, W. E. Comparison of the Acidic Properties of H-[Al]ZSM-5, H-[Fe]ZSM-5, and H-[Ga]ZSM-5 Using Microcalorimetry, Hexane Cracking, and Propene Oligomerization. *J. Phys. Chem.* **1995**, *99*, 8745−8749.
(13) Brandle, M.; Sauer, J. Acidity Differences between Inorganic Solids Induced by Their Framework Structure. A Combined Quantum Mechanics Molecular Mechanics Ab Initio Study on Zeolites. *J. Am. Chem. Soc.* **1998**, *120*, 1556−1570.
(14) Rigby, A. M.; Kramer, G. J.; van Santen, R. A. Mechanisms of Hydrocarbon Conversion in Zeolites: A Quantum Mechanical Study. *J. Catal.* **1997**, *170*, 1−10.
(15) Derouane, E. G. On the Physical State of Molecules in Microporous Solids. *Microporous Mesoporous Mater.* **2007**, *104*, 46−51.
(16) Carr, R. T.; Neurock, M.; Iglesia, E. Catalytic Consequences of Acid Strength in the Conversion of Methanol to Dimethyl Ether. *J. Catal.* **2011**, *278*, 78−93.
(17) Gounder, R.; Jones, A. J.; Carr, R. T.; Iglesia, E. Solvation and Acid Strength Effects on Catalysis by Faujasite Zeolites. *J. Catal.* **2012**, *286*, 214−223.
(18) Skeels, G. W.; Breck, D. W. Silicon Substituted Y Zeolite Composition Lz-210. 4,711,770, December 8, 1987.
(19) Corma, A.; Fornes, V.; Rey, F. Extraction of Extra-Framework Aluminum in Ultrastable Y-Zeolites by $(NH_4)_2SiF_6$ Treatments . 1. Physicochemical Characterization. *Appl. Catal.* **1990**, *59*, 267−274.
(20) Elomari, S. Hydrocarbon Conversion Using Zeolite SSZ-53. 6,841,063, January 11, 2005.
(21) Zones, S. I.; Benin, A.; Hwang, S.-J.; Xie, D.; Elomari, S.; Hsieh, M.-F. Studies of Aluminum Reinsertion into Borosilicate Zeolites with Intersecting Channels of 10- and 12-Ring Channel Systems. *J. Am. Chem. Soc.* **2014**, *136*, 1462−1471.
(22) Lobo, R. F.; Zones, S. I.; Medrud, R. C. Synthesis and Rietveld Refinement of the Small-Pore Zeolite SSZ-16. *Chem. Mater.* **1996**, *8*, 2409−2411.
(23) Zones, S. I.; Zhang, G.; Krishna, K. R.; Biscardi, J. A.; Marcantonio, P.; Vittoratos, E. Preparing Small Crystal SSZ-32 and Its Use in a Hydrocarbon Conversion Process. 7,390,763, June 24, 2008.
(24) Zones, S. I. Synthesis of Pentasil Zeolites from Sodium Silicate Solutions in the Presence of Quaternary Imidazole Compounds. *Zeolites* **1989**, *9*, 458−467.
(25) Emeis, C. A. Determination of Integrated Molar Extinction Coefficients for Infrared Absorption Bands of Pyridine Adsorbed on Solid Acid Catalysts. *J. Catal.* **1993**, *141*, 347−354.
(26) Kresse, G.; Hafner, J. Ab Initio Molecular Dynamics for Liquid Metals. *Phys. Rev. B* **1993**, *47*, 558−561.
(27) Kresse, G.; Furthmüller, J. Efficiency of Ab-Initio Total Energy Calculations for Metals and Semiconductors Using a Plane-Wave Basis Set. *Comput. Mater. Sci.* **1996**, *6*, 15−50.
(28) Kresse, G.; Furthmüller, J. Efficient Iterative Schemes for Ab Initio Total-Energy Calculations Using a Plane-Wave Basis Set. *Phys. Rev. B* **1996**, *54*, 11169−11186.
(29) Kresse, G.; Hafner, J. Ab Initio Molecular-Dynamics Simulation of the Liquid-Metal−Amorphous-Semiconductor Transition in Germanium. *Phys. Rev. B* **1994**, *49*, 14251−14269.
(30) Lee, K.; Murray, É. D.; Kong, L.; Lundqvist, B. I.; Langreth, D. C. Higher-Accuracy van der Waals Density Functional. *Phys. Rev. B* **2010**, *82*, 081101.
(31) Murray, E. D.; Lee, K.; Langreth, D. C. Investigation of Exchange Energy Density Functional Accuracy for Interacting Molecules. *J. Chem. Theory Comput.* **2009**, *5*, 2754−2762.
(32) Blöchl, P. E. Projector Augmented-Wave Method. *Phys. Rev. B* **1994**, *50*, 17953−17979.
(33) Kresse, G.; Joubert, D. From Ultrasoft Pseudopotentials to the Projector Augmented-Wave Method. *Phys. Rev. B* **1999**, *59*, 1758−1775.
(34) Van Koningsveld, H.; Van Bekkum, H.; Jansen, J. C. On the Location and Disorder of the Tetrapropylammonium (TPA) Ion in Zeolite ZSM-5 with Improved Framework Accuracy. *Acta Crystallogr., Sect. B* **1987**, *43*, 127−132.
(35) Olson, D. H.; Kokotailo, G. T.; Lawton, S. L.; Meier, W. M. Crystal-Structure and Structure-Related Properties of ZSM-5. *J. Phys. Chem.* **1981**, *85*, 2238−2243.
(36) Baerlocher, C.; McCusker, L. B. Database of Zeolite Structures. http://www.iza-structure.org/databases/ (accessed January 8, 2014).
(37) Newsam, J. M.; Treacy, M. M. J.; Koetsier, W. T.; Gruyter, C. B. D. Structural Characterization of Zeolite Beta. *Proc. R. Soc. London, A* **1988**, *420*, 375−405.
(38) Materials Studio, 6.0; Accelrys Software Incorporated, San Diego, 2011.
(39) Marler, B.; Deroche, C.; Gies, H.; Fyfe, C. A.; Grondey, H.; Kokotailo, G. T.; Feng, Y.; Ernst, S.; Weitkamp, J.; Cox, D. E. The Structure of Zeolite ZSM-23 (MTT) Refined from Synchrotron X-Ray Powder Data. *J. Appl. Crystallogr.* **1993**, *26*, 636−644.
(40) De Moor, B. A.; Reyniers, M. F.; Gobin, O. C.; Lercher, J. A.; Marin, G. B. Adsorption of C2-C8 N-Alkanes in Zeolites. *J. Phys. Chem. C* **2011**, *115*, 1204−1219.
(41) De Moor, B. A.; Reyniers, M.-F. O.; Sierka, M.; Sauer, J.; Marin, G. B. Physisorption and Chemisorption of Hydrocarbons in H-Fau Using QM-POT(MP2//B3LYP) Calculations. *J. Phys. Chem. C* **2008**, *112*, 11796−11812.
(42) Willems, T. F.; Rycroft, C. H.; Kazi, M.; Meza, J. C.; Haranczyk, M. Algorithms and Tools for High-Throughput Geometry-Based Analysis of Crystalline Porous Materials. *Microporous Mesoporous Mater.* **2012**, *149*, 134−141.
(43) Haranczyk, M. Zeo++. http://www.carboncapturematerials.org/Zeo++.
(44) Madon, R. J.; Iglesia, E. Catalytic Reaction Rates in Thermodynamically Non-Ideal Systems. *J. Mol. Catal. A: Chem.* **2000**, *163*, 189−204.
(45) Baertsch, C. D.; Komala, K. T.; Chua, Y. H.; Iglesia, E. Genesis of Bronsted Acid Sites During Dehydration of 2-Butanol on Tungsten Oxide Catalysts. *J. Catal.* **2002**, *205*, 44−57.

(46) Hunter, E. P. L.; Lias, S. G. Evaluated Gas Phase Basicities and Proton Affinities of Molecules: An Update. *J. Phys. Chem. Ref. Data* **1998**, *27*, 413−656.
(47) Ravenelle, R. M.; Schüβler, F.; D'Amico, A.; Danilina, N.; van Bokhoven, J. A.; Lercher, J. A.; Jones, C. W.; Sievers, C. Stability of Zeolites in Hot Liquid Water. *J. Phys. Chem. C* **2010**, *114*, 19582−19595.
(48) Xu, B.; Rotunno, F.; Bordiga, S.; Prins, R.; van Bokhoven, J. A. Reversibility of Structural Collapse in Zeolite Y: Alkane Cracking and Characterization. *J. Catal.* **2006**, *241*, 66−73.
(49) Bourgeat-Lami, E.; Massiani, P.; Di Renzo, F.; Espiau, P.; Fajula, F.; Des Courières, T. Study of the State of Aluminium in Zeolite-B. *Appl. Catal.* **1991**, *72*, 139−152.
(50) Zecchina, A.; Bordiga, S.; Spoto, G.; Scarano, D.; Spano, G.; Geobaldo, F. IR Spectroscopy of Neutral and Ionic Hydrogen-Bonded Complexes Formed Upon Interaction of CH_3OH, C_2H_5OH, $(CH_3)_2O$, $(C_2H_5)_2O$ and C_4H_8O with H-Y, H-ZSM-5 and H-Mordenite: Comparison with Analogous Adducts Formed on the H-Nafion Superacidic Membrane. *J. Chem. Soc., Faraday Trans.* **1996**, *92*, 4863−4875.
(51) Ramachandran, C. E.; Williams, B. A.; van Bokhoven, J. A.; Miller, J. T. Observation of a Compensation Relation for N-Hexane Adsorption in Zeolites with Different Structures: Implications for Catalytic Activity. *J. Catal.* **2005**, *233*, 100−108.
(52) Eichler, U.; Brandle, M.; Sauer, J. Predicting Absolute and Site Specific Acidities for Zeolite Catalysts by a Combined Quantum Mechanics Interatomic Potential Function Approach. *J. Phys. Chem. B* **1997**, *101*, 10035−10050.
(53) Higgins, J. B.; LaPierre, R. B.; Schlenker, J. L.; Rohrman, A. C.; Wood, J. D.; Kerr, G. T.; Rohrbaugh, W. J. The Framework Topology of Zeolite Beta. *Zeolites* **1988**, *8*, 446−452.
(54) Sklenak, S.; Dedecek, J.; Li, C.; Wichterlova, B.; Gabova, V.; Sierka, M.; Sauer, J. Aluminium Siting in the ZSM-5 Framework by Combination of High Resolution ^{27}Al NMR and DFT/MM Calculations. *Phys. Chem. Chem. Phys.* **2009**, *11*, 1237−1247.
(55) Pophale, R.; Cheeseman, P. A.; Deem, M. W. A Database of New Zeolite-Like Materials. *Phys. Chem. Chem. Phys.* **2011**, *13*, 12407−12412.